Electrochimica Acta 524 (2025) 146012

Contents lists available at ScienceDirect

Electrochimica Acta

journal homepage: www.journals.elsevier.com/electrochimica-acta

Design of a low-cost ultrasonic testing instrument for battery metrology

Sam Amsterdam, Wesley Chang *

Department of Mechanical Engineering and Mechanics, Drexel University, Philadelphia, PA 19104, USA

ARTICLE INFO

Keywords:
Batteries
Ultrasound
Metrology

ABSTRACT

Nondestructive ultrasonic testing is finding increasing use in battery science. We provide instructions and software for the development of a low cost, modular, and easy to use scanning acoustic microscope. Basic principles of ultrasonic testing are discussed with particular attention to its application for *operando* characterization of batteries. An example measurement showing real time monitoring of electrolyte wetting in a pouch cell is shown. By providing detailed hardware setup instructions and freely available analysis software, this paper aims to make ultrasonic testing accessible to the wider battery research community.

1. Introduction

Nondestructive measurement of batteries under operating conditions is essential to the production of next generation electrochemical energy storage technologies [1–3]. This is important for a number of reasons: for fundamental understanding of battery material evolution under cycling [4], for advanced manufacturing and metrology in factories [5–7], and for improved measurement accuracy of state-of-charge (SoC) and state-of-health (SoH) in battery management systems (BMS) [8].

A variety of techniques exist to address this need, each with tradeoffs in cost, space and time resolution, and ease-of-use such that no single measurement can accessibly address all requirements simultaneously. For example, X-ray computed tomography (CT) can nondestructively produce a 3D image of a battery with high spatial resolution, but requires expensive equipment, longer measurement times, and computationally intensive analysis [9]. Electrochemical impedance spectroscopy (EIS) by contrast, is much more accessible to battery researchers but does not provide spatially resolved information and requires careful model building in order to provide useful information [10].

Ultrasound has emerged as a promising tool for overcoming a number of shortcomings in the battery research field [11,12]. The technique analyzes the interaction of high frequency acoustic pulses with a battery to gain information about the coupled electrochemical and mechanical changes that occur during cycling [13–15], wetting [16], and failure [17–20]. While most published studies use pouch cells with solid electrodes and liquid electrolytes, ultrasound can be applied to any chemistry or form factor, including solid-state [21], redox flow batteries [22], or cylindrical cells [23].

When the ultrasonic transducers are mounted on a motorized gantry that rasters across a sample, spatial resolution on the order of ~100 μm and time resolution of milliseconds is routinely achievable, a technique called scanning acoustic microscopy (SAM). This testing does not interfere with cycling or other testing of a cell, meaning it can be coupled with other techniques such as EIS to provide complementary information. Commercial SAM instruments cost tens to hundreds of thousands of dollars, making them a risky investment for a battery research group that likely has minimal experience with ultrasound.

In this paper, we present the design of a low cost, easy to use SAM built from widely available hardware. We have also written free, open-source software which runs the instrument and enables high speed analysis of the resulting data. We hope that by lowering the barrier to entry, ultrasonic testing can become a routine part of battery characterization available to any research group in the field.

2. Materials and methods

2.1. Battery fabrication

Our ultrasonic system was validated using 250 mAh battery pouch cells that were machine-made (Li-Fun) with lithium manganese iron phosphate (LMFP) cathodes and copper current collectors as the bare anode, and shipped to us dry. All fabrication steps were carried out in an inert atmosphere glove box (Argon, $O_2 < 0.5$ ppm, $H_2O < 0.1$ ppm). Electrolyte was prepared by making a 1:1 volume/volume (v/v) mixture of diethyl carbonate (DEC) (Acros Organics) and fluoroethylene carbonate (FEC) (TCI). Lithium difluoro(oxalato)borate (LiDFOB) (Sigma

* Corresponding author.
E-mail address: wc552@drexel.edu (W. Chang).

https://doi.org/10.1016/j.electacta.2025.146012
Received 20 December 2024; Received in revised form 5 March 2025; Accepted 9 March 2025
Available online 10 March 2025

Aldrich) powder was weighed and then dissolved in the 1:1 (v/v) DEC: FEC solvent at a 2 M concentration by overnight stirring. The dry pouch cells were cut open in the glovebox and further dried in the glovebox antechamber under vacuum at 120 °C to remove residual moisture. 1.00 mL of the 2 M LiDFOB in 1:1 (v/v) DEC:FEC was added to the cell. The pouch was then vacuum sealed at −90 kPa and immediately removed from the glovebox for ultrasonic testing.

2.2. Battery ultrasonic testing and electrical measurements

The cell was placed in a custom-made pressure application jig with hard plastic plates. The battery was mounted at the edge of the plates in order to allow easy access to the metal current collecting tabs. The pressure jig with battery was then immersed in a water bath with the water level just below the edge of the current leads, and the whole setup placed on the home-built SAM to enable ultrasonic measurement. The battery was connected to a potentiostat (Admiral Instruments Squidstat Plus) and open circuit voltage (OCV) and EIS were measured every 30 min for three days. EIS was measured at open circuit with a 10 mV amplitude at a frequency range of 1 MHz to 1 Hz with 10 measurements per decade. SAM images were measured using 2.25 MHz transducers rastered over a 27.0 mm by 27.0 mm square with 0.5 mm step size, repeated every 30 min. Each ultrasonic wave was sampled 1000 times over a 16.000 μs period (16 ns time resolution) with an 18.000 μs delay from pulse start to measurement start. The measurement at each pixel in the scan was repeated 1000 times and the average of these measurements saved.

2.3. Measurement principles

The basic principles of ultrasonic measurements are presented in this section. Further details and more advanced topics can be found in a number of texts [24,25]. The general idea is to produce a high frequency acoustic wave (200 kHz – 50 MHz range for batteries) [26,27], allow the wave to interact with a sample, and measure the resulting acoustic signal. By observing how the sound wave has changed upon interacting the sample, we can deduce a number of structural and mechanical features of the sample.

There are three primary measurement geometries of an ultrasound experiment: transmission, pulse-echo, and pitch-catch (Fig. 1a). In a transmission measurement, one ultrasonic transducer is used to produce the sound wave, which goes through the sample and is measured on the other side by a receiving transducer. In pulse-echo mode, the same transducer is used to send in the ultrasound and measure the signals that are reflected off the sample. In pitch-catch mode, the sending transducer is placed at an angle to the sample and the reflected waves are measured by a similarly angled transducer.

In terms of instrumentation and analysis, transmission is the most straightforward. In many circumstances, the earliest measured signal is also the strongest and does not contain internal reflections. Later arriving signals are possible in transmission due to multiple internal reflections, but these are almost always lower intensity and easy to separate from the primary wave. In pulse-echo and pitch-catch measurements, the measured signals are due to reflections at interfaces within the sample. This contains richer information, with increasing time delays giving a depth profile of the sample, but at the cost of more difficult analysis since these signals are often overlapping and difficult to deconvolute and interpret.

For practical experiments, each geometry has unique considerations. Transmission measurements are again the most straightforward: separate pulse and measure transducers mean that no extra filtering is required to separate the high voltage (> 100 V) pulses from low voltage (<0.5 V) signals. Pitch-catch measurements have similar simplicity in the signal acquisition, but have the added difficulty of requiring proper angle alignment between the pitching and catching transducers. Since pulse-echo measurements use a single transducer to both generate the ultrasonic pulse and measure the reflected signals, care must be taken to prevent the high voltage pulse from interfering with the low voltage signal. The pulse generator used in this setup can filter and amplify this signal, but this process does induce some distortion in the wave that needs to be corrected. An example of this correction process is included in the Discussion section. In addition, it is often useful to introduce a delay between the pulse and measurement, either by moving the transducer further from the sample or by using specialized delay-line transducers.

Given the advantages and drawbacks of these geometries, it is often

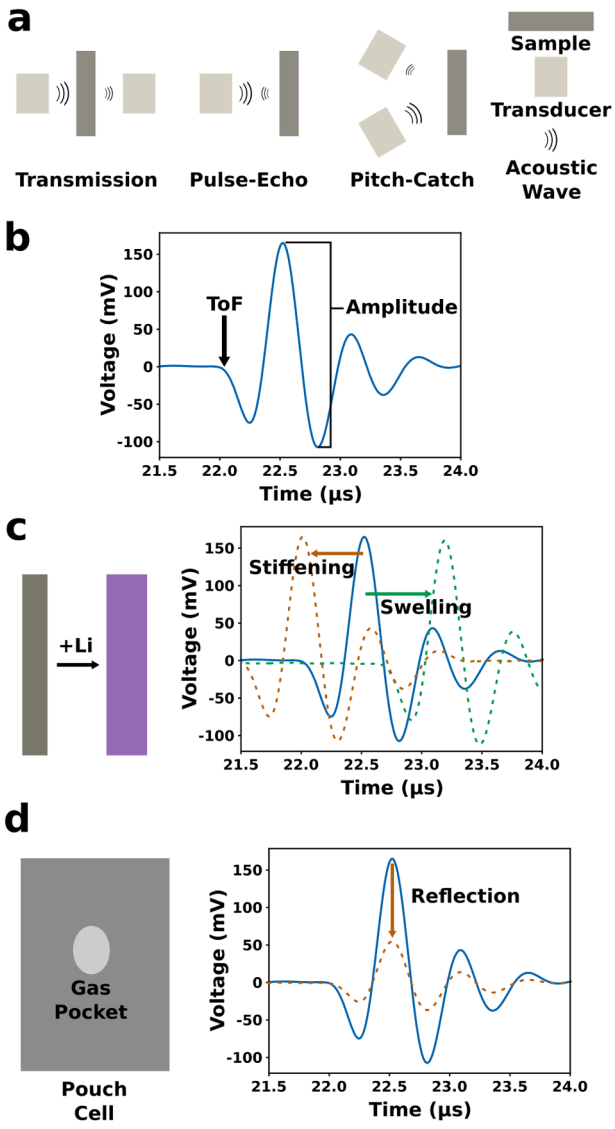

Fig. 1. (a) The three measurement geometries used in ultrasound measurement. (b) An example ultrasonic transmission waveform produced by a 2.25 MHz pulse. The time of flight (ToF) and amplitude are highlighted. (c) Schematic representation of a graphite anode swelling and changing modulus upon lithium intercalation, and the corresponding effect on the pristine graphite (blue) that swelling (dotted green) and stiffening (dotted orange) would have in isolation on the transmission ToF. Note that an actual experiment would be the sum of these effect on the ToF and would also show a change in amplitude. For lithium intercalation into graphite, the overall effect is a decrease in ToF since the relative change in modulus is greater than the relative change in thickness [14]. (d) Schematic representation of a gas pocket forming within a battery and the effect of the reflective interface this creates on the transmission amplitude. The solid blue line represents the normal transmission and the dotted orange line the transmission through a gas pocket. Note that in a real measurement the ToF may also change due to the different speed of sound of the gas.

useful to combine different collection methods. The software presented in this article provides support for a multiplexer which enables a user to perform measurements in multiple configurations simultaneously.

The rest of this section will sketch out the basic relations that enable an experimenter to calculate physical properties of a sample from the measured properties of an ultrasonic wave. It should be noted that most of these derivations assume that the acoustic wave is normal to the sample; for angled measurements in a pitch-catch geometry, deeper analysis requires consideration of the angle of incidence. More detail of the physics and mathematical details of these derivations can be found in [24].

For the purpose of analysis, two parameters are often extracted from an ultrasound signal: the time of flight (ToF) and the amplitude, shown on an example waveform in Fig. 1b. ToF represents the total travel time of the acoustic wave between its emission from the pulsing transducer and its measurement at a receiving transducer. The amplitude is a measure of the intensity of the voltage output from a piezoelectric transducer and is directly proportional to the pressure on the transducer and its area. The wave maximum or span (maximum - minimum) are common metrics for the amplitude. Within the battery field, a common experiment is to cycle a battery or perform other electrochemical characterization while simultaneously probing the battery by ultrasound. This enables an experimenter to establish a relationship between the battery properties, such as SoC or SoH, and the ultrasound metrics like ToF or amplitude. This relationship is typically empirical [14], though recent efforts have made progress towards relating battery chemomechanics and state through direct analysis of ultrasound [28].

The total ToF through a sample is determined by the distance the wave travels through the sample and the speed of sound within the sample. If the thickness of a sample can be measured, the speed of sound of the sample can be calculated. This in turn is related to the Young's modulus (E) and density (ρ) of the sample by

$$v = \sqrt{(E/\rho)} \tag{1}$$

For porous materials this relation is more complicated. It is tempting to assume the density in Eq. (1) could be treated as a porosity weighted sum of the fluid and solid components, and thus it would be possible to extract the porosity value of an electrode film through a simple speed of sound measurement. This is unfortunately not correct: propagation of a wave through a poroelastic medium must be analyzed through the framework of Biot Theory or related approaches [29]. Without this type of analysis, the speed of sound measurement would give an effective or 'acoustic density' that may be empirically useful, but not directly related to porosity.

For most measurement setups, the sound wave will need to travel through several different materials, and the measured ToF is the sum of the ToF through each component. In order to isolate the ToF of one component of a measurement setup, two approaches can be taken. One is to measure the thickness of each component and use known speeds of sound whenever possible (e.g. for water when used as a coupling fluid) in order to calculate the portion of the ToF due to the component of interest. Another possibility is to combine measurement modes: a combination of transmission and pulse-echo measurements, for example, can be used to isolate the ToF of a sample from the ToF due to surrounding coupling fluid. The method is explained in more detail later.

It is also important to remember that ToF as a metric is sensitive to changes in both the distance traveled and the speed of sound within a sample. Therefore a change in ToF through a battery could point to changes in a component's thickness, density, or stiffness. These changes are often coupled – a material may both swell and decrease in modulus during cycling, causing an increase in ToF. An example of the competing effects of material stiffening and swelling on ToF are shown in Fig. 1c.

Determination of ToF from a waveform can be done through a number of algorithms. The two that are currently implemented in the software are the short time average / long time average (STA/LTA) method and the envelope threshold method. In the STA/LTA method, two rolling averages are calculated along the waveform, one with a short time window and one with a longer time window. The ToF is taken to be the point where the ratio of these two averages exceeds a threshold value. It is up to the experimenter to define the length of the short window, long window, and the threshold value such that the algorithm consistently picks the start of the wave. In the envelope threshold method, the wave envelope is calculated by taking the magnitude of the Hilbert transform. The ToF is then defined as the time when the wave envelope exceeds a certain fraction of the maximum value of the envelope. The experimenter must choose a threshold fraction that is sensitive (to get the soonest possible arrival time) but does not lead to false positives (identifying noise as the arrival time). Many other algorithms are used in the literature, each with tradeoffs in accuracy and robustness. Fine tuning an algorithm's parameters can be time consuming but is necessary to reliably calculate ToF.

Analysis of the amplitude of the measured wave also provides valuable experimental information. Waves propagating through a medium lose intensity due to absorption and scatter with an exponential decay over distance:

$$P = P_0 exp(-\alpha \Delta x) \tag{2}$$

where P is the acoustic pressure measured at point x, P_0 is an initial pressure at a reference point, Δx is the distance from the reference point and α is an attenuation coefficient. The attenuation coefficient is usually reported in decibels per distance and can be measured experimentally by performing a transmission measurement through different thicknesses or distances in a material.

Scatter can be a large contributor to attenuation loss. Typical ultrasound frequencies used in battery metrology are in the 200 kHz – 50 MHz range [26,27]. The corresponding wavelengths (hundreds of microns at the MHz range) are much larger than the typical particle size (20 μm or less) in an electrode, meaning that Rayleigh scattering dominates. As a result, scattering losses dramatically increase at higher frequencies and there is a tradeoff when choosing the frequency in an experiment: higher frequencies can provide better spatial and temporal resolution to measurements, but at the cost of signal intensity and penetration depth.

Like many related material parameters, attenuation coefficients are sensitive to measurement conditions (i.e. temperature, dissolved species concentration) as well as processing (particle size and calendaring in particle films). In addition, performing thickness-dependent amplitude measurements is challenging for many air-sensitive battery components. As a result, it is usually infeasible to know the attenuation coefficient of the components in a battery and an experimenter is usually concerned with relating a change in amplitude to a change in attenuation, rather than measuring the absolute value of the attenuation coefficient.

In addition to absorption and scattering losses, amplitude can also be lost at interfaces between materials. When considering an acoustic wave moving through an interface between two different materials, it is useful to consider the acoustic impedance Z, defined as

$$Z = \rho v \tag{3}$$

where ρ is the material density and v is the speed of sound. When an acoustic wave encounters an interface, the velocity, acoustic pressure and phase of the wave must be continuous across the interface. These conditions allow the calculation of the ratio of reflected and transmitted acoustic pressure as a wave moves from a material of impedance Z_1 to a material of impedance Z_2 at normal incidence:

$$r = P_r/P_i = (Z_2 - Z_1)/(Z_2 + Z_1) \tag{4}$$

$$t = P_t/P_i = 2Z_2/(Z_2 + Z_1) \tag{5}$$

where P_r, P_t, and P_i are the reflected, transmitted, and incident acoustic

pressures. Careful analysis of ultrasonic signals, along with prior knowledge of the system being measured, enable an experimenter to calculate these transmission and reflection coefficients and from them deduce a sample's acoustic impedance, density, and velocity. Note also that these relations only hold for normal incidence. Calculation of t and r from pitch-catch measurements requires more advanced analysis which is covered in more detail in [24].

It should be noted that t and r are not restricted to the range of 0 to 1. If Z_2 is less than Z_1, r will be negative, resulting in a change of the sign of the reflected wave. If Z_2 is greater than Z_1, t will be greater than 1, resulting in a greater pressure transmitted than incident on the interface. While this may initially be counterintuitive, it does not violate conservation of energy and is a natural consequence of the continuous velocity condition at the interface. A qualitative explanation is that Z_2 is the 'harder' material and Z_1 is the 'softer' material. The displacements at the interface must be equal due to the boundary conditions, but an equal magnitude displacement will result in a greater acoustic pressure in the harder material.

Eq. (4) and Eq. (5) show that amplitude is a particularly sensitive measurement for gas formation in a battery [18]. The acoustic impedance of most gases is on the order of hundreds of Rayl (1 Rayl = 1 kg/m^{2}s), while solids and liquids are typically greater than 10^6 Rayl. This means a solid/gas interface will have a reflection coefficient >0.99. An ultrasonic wave encountering a solid-gas or liquid-gas interface will have most of its amplitude reflected, shown schematically in Fig. 1d.

In addition to ToF and amplitude, more advanced signal processing and modeling can be employed to further analyze the battery. The measured ultrasonic signal is rich with information about the chemo-mechanical properties of every component of the battery under test, but deconvoluting and analyzing this information requires more advanced analysis beyond the scope of this paper. These methods include Fourier analysis [15], wavelet transforms [30], and advanced modeling [28].

2.4. Measurement hardware

The instrument we show here is designed to be modular, with increasing complexity (and cost) enabling more types of measurements. An example setup is shown in Figure S1. A summary of the required and optional hardware, their purpose, and approximate cost can be found in Table 1. The most basic setup requires a computer, a pulser, an ultrasonic transducer, and an oscilloscope. The pulser generates a high voltage, short duration pulse which is fed to a piezoelectric transducer, generating the ultrasonic wave. After interacting with the sample, the wave is then picked up by the same transducer (pulse-echo mode) or a different one (transmission or pitch-catch) and the resulting voltage signal measured by an oscilloscope. This process is repeated and the results averaged to produce the measurement reported on the computer. The connection of the hardware components determines what kind of measurement is performed – examples of basic transmission and pulse-echo measurements are shown in Figs. 2a and 2b, respectively.

The frequency of the ultrasonic pulse can be programmatically changed in the pulser, but the actual frequency that is produced is largely determined by the transducer. The construction of the transducer (i.e. its shape and materials) determines the range of frequencies it can efficiently produce and measure. Generally, an ultrasonic pulse frequency should match the central frequency of the transducer material, and a large mismatch will result in little to no measurable signal. Multiple transducers with different central frequencies are usually needed to measure over a wide frequency range. In addition, focused transducers that shape the resulting acoustic wave to a single line or point are also available. Use of these transducers for 3D mapping of batteries is an active area of research [17].

We provide support for two different pulser models. The standard pulser emits a single short pulse with a shape similar to a Morlet wavelet (a sinusoidal oscillation bounded by a Gaussian window). The other option is a tone burst pulser, which ideally emits a sinusoidal wave with a variable number of periods (half-cycles) set by the user, up to 16. Tone burst pulsers are able to deliver a larger total energy in the ultrasonic wave but require longer measurement times due to their generally lower pulse repetition frequency (PRF). Due to software and hardware implementation details, the tone burst pulser discussed here only works on Windows computers and cannot be used for pulse-echo measurements.

Efficient data collection from the oscilloscope is key to making fast, low-noise measurements. The Picoscope is run in 'rapid block mode', which instructs it to store measurement data locally in pre-defined memory blocks every time it is triggered by a timing pulse from the pulser. Only after the measurement is repeated a user-defined number of times does the data get transmitted to the computer. This enables measurement speed to be limited by the PRF and the transit time of the wave rather than data transmission and saving times. Collecting 5000 waveforms per second is routinely achievable, making high signal to noise measurements obtainable with little time overhead. One limitation of rapid block mode is that the total measurement – the number of data points in a wave times the number of waves being averaged - is limited by the oscilloscope memory. As a result, preliminary measurements are often performed in order to determine the time range of interest and then the measurement is repeated within that narrower time range with a higher sampling (i.e. better time resolution but more memory consumption). In a typical transmission measurement using a 2.25 MHz transducer, a measurement range of 2–4 μs is used at the maximum time

Table 1
Required and optional hardware for ultrasonic testing and their approximate cost. If a piece of hardware has 'All' in the Experiments Enabled column, it is required to do any experiment and represents the baseline requirement.

Instrument Type	Manufacturer	Model	Approximate Cost (USD, 2024)	Experiments Enabled	Notes
Computer	Any	Windows recommended, Ubuntu also tested	>200	All	Requires at least 4 USB ports
Pulser	Ultratek	CompactPulser	4785	All	Requires Serial port/USB adapter
Tone Burst Pulser	Ultratek	USB-UT350	6540	Tone burst pulsing	Requires purchasing software SDK from Ultratek. Only compatible with Windows
Oscilloscope	Picotech	2208B (two channel 100 MHz bandwidth)	825	All	Associated Python module requires manual installation. Only model 2208B is currently supported
Transducer	Olympus	Videoscan V133-RM (2.25 MHz central frequency)	350	All	Any frequency, size, and focal arrangement of transducer can be used as long as it 1) connects via BNC cable and 2) is within the frequency range of the pulser
Gantry	Creality	Ender-3	250	Scans	Requires removal of printer head to function as a gantry
Multiplexer	Cytec	CXAR 16/M-F (two 8×1 modules)	2000	Multimodal (transmission and pulse-echo) measurement	Requires 2 switch modules, USB connection, BNC to BNC connectors and adapter. The number of switches and module design is fully customizable
Transducer Holder			5	Scans	3D printed Example files are available

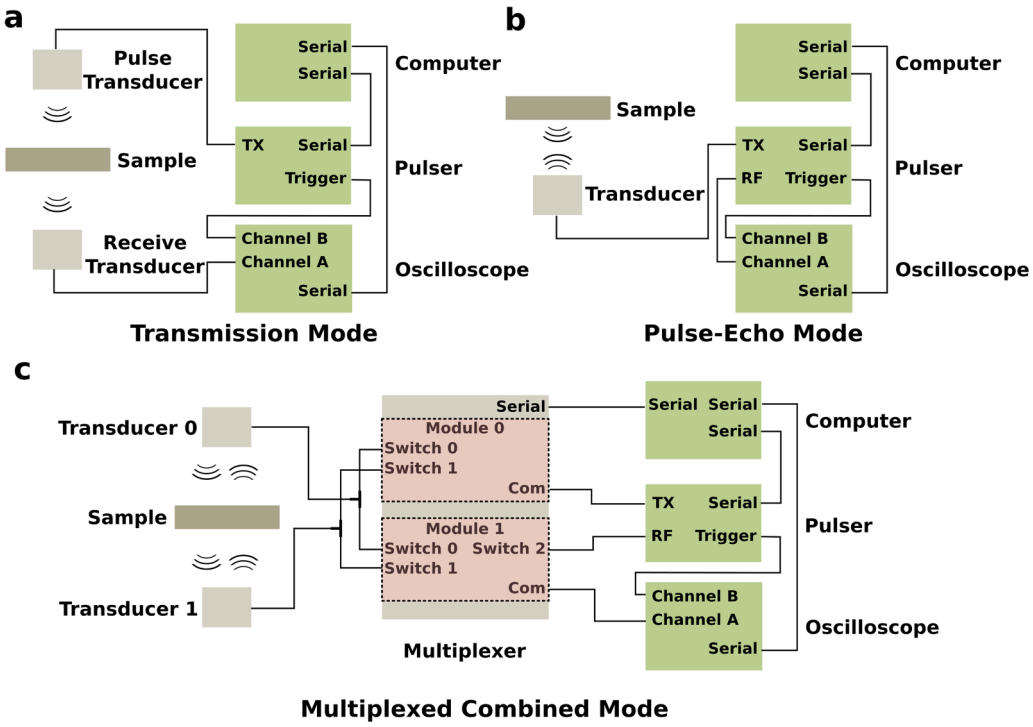

Fig. 2. Wiring diagrams for (a) transmission, (b) pulse-echo, and (c) multiplexed measurements. All lines are Bayonet Neill Concelman (BNC) cables except connections between serial ports, which use USB cables with appropriate adapters. Thicker lines on the cables in panel (c) denote BNC T-junctions. Note that pitch-catch measurements would use the same wiring as transmission measurements.

resolution of 2 ns (1–2000 data points per measurement) and averaged 10–10,000 times. At maximum PRF a measurement has an initialization time of 5–10 ms and each averaged waveform adds about 300 μs to the measurement time (Figure S2a).

Pulse-echo measurements require using the Ultratek Compact Pulser (not the tone burst pulser), which has a built-in filter and amplifier for separating the high voltage pulse from the much lower amplitude signal that runs on the same line. This unfortunately results in a large and varying background in the first few microseconds of the measurement that must be corrected to properly interpret pulse-echo measurements. Background correction is performed post-measurement within the software, and the user can define their own correction protocol. Measurements performed with a sufficient delay, either by moving the transducer further from the sample or using a specialized delay-line transducer, may only need a linear background subtraction if the amplifier background is small enough. In cases where this is insufficient, we have found a high-pass Butterworth filter with a critical frequency of 10 % of the transducer frequency, followed by a linear background subtraction to be adequate for this purpose. This has been tested with measurements at 2.25 MHz and 50 MHz by comparing the shape of the pulse-echo measurement to a reference transmission wave to check for distortions to the wave shape. This process may become less robust at lower frequencies that begin to overlap with the amplifier background. A more rigorous quality check would involve a comparison of the signal power spectrum before and after filtering to test for the presence of background distortions near the Butterworth cutoff frequency. In addition, comparison of amplitude between different measurements requires a correction for the amplifier gain, which can vary depending on signal optimization protocols.

SAM requires that the transducer be rastered over the sample. This is done by 3D printing holders for the transducers and mounting them on a 3D printer gantry with the print head removed. Scan measurements are then performed by measuring at user-defined increments in a 2D area. Lateral motion in 100 μm increments are possible in this setup, with better resolution possible using higher frequency transducers and a more precise (but higher cost) gantries. Scan speed will depend heavily on experiment parameters. Using the example parameters from the paragraph above (2000 samples per wave, averaging 1000 times per measurement), a 25 x 40 mm at 0.5 mm increments (4000 total pixels) takes about 30 min. This speed can be increased by reducing the number of samples or number of waves being averaged: a similar measurement area averaging 1000 data points 10 times per pixel will scan in about 5 min (Figure S2b). Analysis of the noise in transmission measurements show that averaging 10 measurements per pixel is sufficient to reduce the background noise to below 1 mV (Figure S2c-f). A future goal is to implement faster scanning modes such as streaming (measurement while the scanner is constantly moving) and parallel collection (using multiple transducers in parallel) in order to further reduce measurement times.

In order to achieve a high resolution signal, special care must be taken in the coupling of the ultrasonic transducers to the battery being measured. In non-scanning measurements, the transducers can be directly clamped to a battery with a coupling gel on the interface. For scanning measurements, the battery and transducers are usually submerged in a coupling fluid such as water or mineral oil. Specialized air-coupled transducers may also be used to avoid liquid couplant, but these suffer from very high signal attenuation and are unlikely to be suitable for transmission measurements through pouch cells. Bubbles and temperature fluctuations in the coupling fluid can cause variations in measurements and should be avoided. Certain battery chemistries, such as lithium metal cells, require a pressure jig for optimal cycling performance. Ultrasonic measurements can be made through such setups, provided that the plates of the pressure jig are made of a hard plastic rather than a metal since the high acoustic reflectivity of metal plates in a fluid tends to overwhelm signal from the battery. Since density and elastic modulus (and therefore speed of sound) are a function of applied pressure, the jig should be secured with compression springs and a torque wrench to ensure reproducibility.

A multiplexer is another useful but not required hardware addition that is supported by the software. This allows rapid switching between

different measurement directions and modes, i.e. front-to-back transmission followed by pulse-echo from the back side of the sample. While this is technically possible with only the pulser and oscilloscope, it requires manual rewiring for each change in direction or measurement mode. With a multiplexer, this change can be done quickly and automatically, enabling multimodal scans without user intervention. An example wiring diagram that enables all combinations of direction and transmission/pulse-echo is shown in Fig. 2c. Note that care must be taken when setting up multiplexed measurements to avoid directly connecting the pulser TX output to the oscilloscope. Excitation pulses are up to 300 V, which is well outside the safe operating range of the oscilloscope and will damage it. The software will check that a given module/switch combination for a measurement is safe, but this depends on the user-entered addresses matching the physical wiring.

2.5. Software

Instrument control software is written in Python and available on GitHub [31]. The pulser, gantry, and multiplexer are controlled via serial commands, while the oscilloscope uses a software developer kit (SDK) provided by Picotech. It should be noted that the oscilloscope and pulser commands are specific to the make and model of the instrument. We can only guarantee the multiplexer and scanner code is compatible with the Cytec CXAR/16-MF (with a switch and control 8×1 module) and Creality Ender-3 3D printing gantry, respectively, but it is likely to be broadly compatible with any Cytec multiplexer and serial-enabled gantry that operates on GCode. Adding more instrument options is a long-term goal but as of the writing of this article only the listed hardware can be used.

The software can be run either through a script or a graphical user interface (GUI). Ultrasound parameters that are user-facing include the transducer frequency, the measurement duration and start time after pulsing, as well as sampling rates and number of waves to average per measurement. In addition, the number of half cycles in a tone burst pulse can be altered. Measurements can be performed at a single location either once or repeatedly, or spatially resolved scans can be performed. There is also an option to automatically identify the optimal oscilloscope voltage range and, if measuring in pulse-echo mode, voltage offset and amplifier gain to maximize signal fidelity. This auto-ranging feature repeats the specified measurement until the optimal parameters are identified and will adjust if they change during a measurement. This feature enables the gathering of high quality data from samples with widely varying amplitude with minimal computational expense.

The software can save data in a number of formats, but we would like to draw particular attention to the pickle, which saves a Python dictionary containing the data as a binary file. While this is no longer human readable in its raw form (vs JSON or a CSV file), it is significantly more optimized for loading and analysis speed. For larger datasets of several hundred files this cuts the speed of analysis and plotting from hours to seconds. Care must be taken to only load pickle files from known sources – malicious executable code can be embedded in a pickle file [32]. The major drawback of the pickle format is that it loads the entire file at once and cannot break up files into smaller chunks. As a result, data is saved during experiments as an SQlite database to avoid memory limits or time overhead associated with repeated save/load cycles. At large enough data sizes (i.e. when the size of individual files to analyze approaches the computer's memory), SQlite becomes the faster method and should also be used for analysis. We note that this situation is unlikely to arise in normal usage but could be possible for large scans with long measurement times and very high time resolution.

A number of basic analysis tools are included in the software. This includes calculation of commonly used metrics such as the maximum wave amplitude and various methods of measuring ToF. A general code wrapper is also provided to efficiently apply user defined analysis functions to large data sets. Results of these metrics are also saved with the data as they are calculated, eliminating the need to redo calculations between sessions. Some basic plotting functions are also provided. Example work flows of loading, analyzing, and plotting data are provided on the GitHub repository [31].

3. Results and discussion

A number of calibration measurements were made to ensure that the testing apparatus works as intended. First, the effect of transducer alignment on transmission measurements was investigated. Fig. 3a shows the output waveform from the pulser and example measurements from well aligned and misaligned transducers. It is evident that misalignment can impact the shape, timing, and amplitude of the wave. We suggest for each combination of transducer, holder, and coupling fluid that a reference waveform is saved. When setting up a new measurement, it is recommended that a blank measurement is collected and compared to the reference to ensure proper alignment.

Another source of experimental error is temperature [33]. The density of most materials changes with temperature, which in turn can affect its speed of sound and thus the measured ToF. The amplitude of a wave may also be affected by temperature. Since acoustic impedance is also a function of density, the impedance mismatch between different materials may change, causing changes in the reflection and transmission coefficients. Fig. 3b shows the variation in the signal ToF and amplitude as temperature varies over two days in the lab. The lab temperature varies on a roughly 24 hour cycle, which causes variations in the measured acoustic properties of the water. For longer timescale measurements, or to directly compare measurements taken at different times, it is recommended that a water 'blank' be included in the measurement to benchmark temperature effects. For more precise measurement, some form of temperature control such as an immersion circulator/thermostat is recommended.

To verify the accuracy of the instrument, a test measurement was performed on an aluminum plate to measure its speed of sound. Transmission and pulse-echo measurement were performed on an aluminum plate 6.54 mm thick (measured by a micrometer) immersed in water using 2.25 MHz ultrasonic pulses (Fig. 3c). Speed of sound is calculated by determining the ToF through the plate alone by separating the ToF through the water by:

$$ToF(Al\ plate) = ToF(Transmission) - ToF(forward\ echo)/2 - ToF(reverse\ echo)/2 \quad (6)$$

The waveforms used to calculate these values are shown in Fig. 3d and their corresponding ToF was calculated by the envelope method with a 10 % threshold. The speed of sound is then calculated by dividing the plate thickness by *ToF(Al plate)*. This gives a value of 6230 m/s, close to the literature value of 6320 m/s [24]. This method is more accurate than directly measuring the transmission ToF using transducers directly clamped to the plate because it eliminates near surface interference effects as well as contributions from the instrument response time (e.g. wave transit time within the transducers themselves).

To demonstrate the use of ultrasound in battery metrology, we monitored the electrolyte infiltration and wetting in a pouch cell. Electrolyte wetting is a significant time bottleneck in manufacturing, requiring hours or even days before formation cycling can commence. Development of fast, nondestructive methods to measure wetting is an active area of research [34]. Ultrasound has already been shown to be well suited to this task [16].

Electrolyte was added to a commercial pouch cell, which was then vacuum sealed and immediately mounted in a plastic pressure jig and measured by EIS and SAM every 30 min for several days. Fig. 4a shows SAM images of the pouch cell (optical image in Fig. 4b) at various time points after electrolyte has been added. As expected, when the liquid electrolyte fills pores and displaces the gas inside the cell, the transmission amplitude increases due to the lower reflection coefficient of the solid/liquid versus solid/gas interface [16]. Within an individual scan,

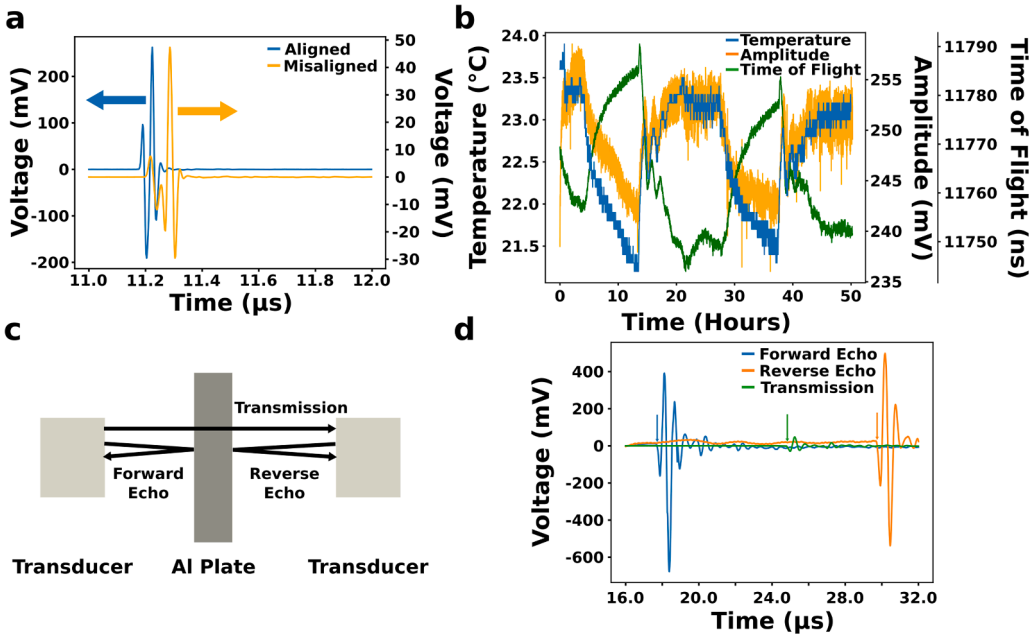

Fig. 3. (a) Example waveforms from aligned and misaligned 50 MHz transducers in water. Note that the aligned and misaligned waveforms use different y-axis scales to emphasize their difference in shape and amplitude. (b) Effect of laboratory ambient temperature on the ToF and amplitude of 50 MHz ultrasound through water. Temperature is measured in air in the same room as the measurement and varies on a 24 hour cycle. (c) Schematic of the measurements used to determine the speed of sound within an Al plate. Arrows indicate the wave path that determines the ToF for each measurement. (d) Waveforms measured in the experiment shown in (c). Arrows on each waveform indicate the measured ToF used to calculate the speed of sound. The pulse-echo waveforms have been corrected by a high-pass filter and a linear baseline subtraction before plotting.

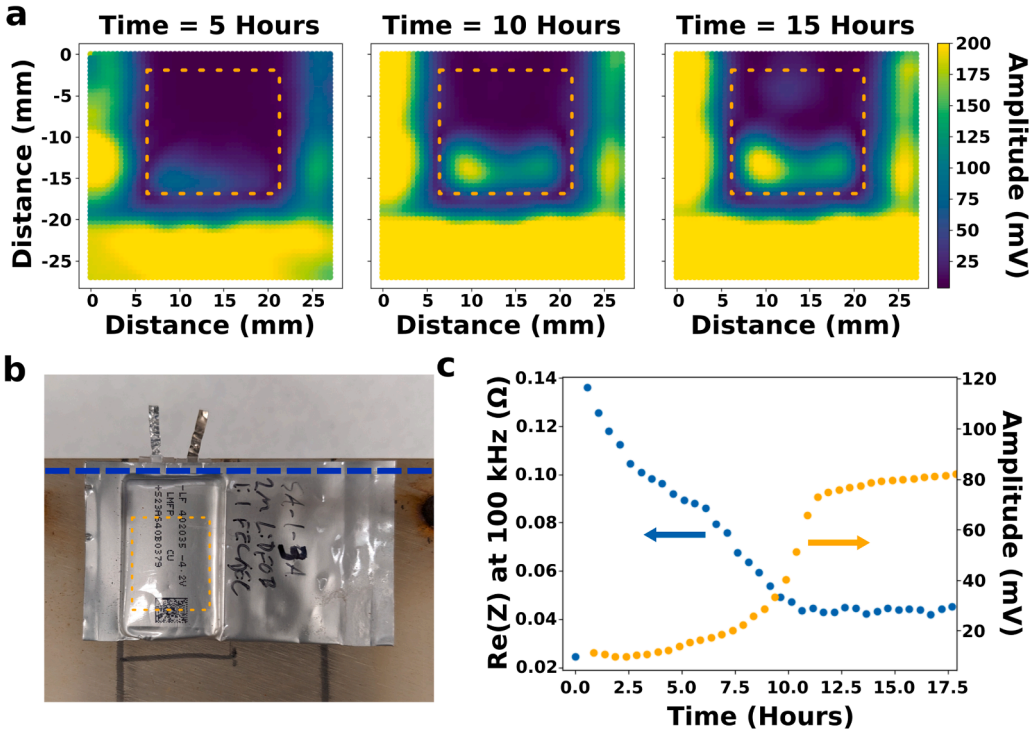

Fig. 4. (a) Representative SAM images of a lithium manganese iron phosphate/copper (LMFP/Cu) battery pouch cell following addition of 1.00 mL of electrolyte. The dotted orange line represents the area of the image that is averaged in (c). Note that the area does not extend all the way to the top to avoid effects of water evaporation that cause intensity fluctuations at long scan times. (b) Image of the pouch cell scanned in (a) on one of the plastic pressure jig plates. The dotted blue line represents the water level during measurements and the dotted orange line is the area averaged in (c). (c) High frequency resistance extracted from EIS and the transmission amplitude (wave maximum – minimum) from ultrasound. Both metrics appear to be highly correlated to the propagation of electrolyte wetting.

amplitude variations at different locations may also arise due to inconsistencies in the contact between the cell and the plastic pressure jig in addition to differences in degree of wetting. As a result, it is more reliable to consider changes over time at a specific pixel or averaged over an area. Another method to reduce this variability is to consider the relative change at each pixel. This is shown in Figure S3. While this introduces other distortions to the amplitude images, this analysis corroborates the results that consider the absolute amplitude. These spatial variations can be reduced by using rubber pads to hold the cell (or not using any pressure jig when possible), but some spatial variance is unavoidable due to inhomogeneities in the cell itself due to e.g. metal current collector tabs. Using SAM to map these inhomogeneities may be useful in future studies.

Since SAM is an *operando* technique, we are able to simultaneously perform EIS measurements on the cell. Fig. 4c shows the high frequency resistance extracted from EIS, a value that is shown to be inversely correlated to the degree of electrolyte wetting [35], as well as the averaged amplitude across the cell area. These values are very well correlated, indicating that ultrasonic amplitude changes are indeed reflective of electrolyte wetting, and that the bulk of the wetting occurs within the first 12 h. We further note that the amplitude continues to change for several hours after the EIS high frequency resistance has reached a steady state, indicating that further chemo-mechanical changes are occurring within the cell that are not captured by the EIS measurement. Further investigation of this effect will be performed in a later study.

4. Conclusion

We demonstrate a low cost, easy to use ultrasonic testing apparatus. The hardware is available for less than $10,000 USD (2024) and we have made the software to run experiments and analyze data freely accessible. We demonstrate the utility of this system by measuring the wetting of electrolyte in a pouch cell by ultrasound and complementary EIS simultaneously. Recognizing the challenge of cross-field technique translation, we hope that this work will lower the barrier of entry for other battery and electrochemistry research groups into non-destructive evaluation and mechanical testing, and to encourage the broad use of ultrasonic testing in routine experimental characterization of batteries.

CRediT authorship contribution statement

Sam Amsterdam: Writing – review & editing, Writing – original draft, Software, Investigation, Formal analysis, Data curation, Conceptualization. **Wesley Chang:** Writing – review & editing, Supervision, Resources, Project administration, Methodology, Funding acquisition, Conceptualization.

Declaration of competing interest

The authors declare that they have no known competing financial interests or personal relationships that could have appeared to influence the work reported in this paper.

Acknowledgements

The authors thank Dr. Randall Leising and Dr. Yunya Zhang at SES AI for fruitful conversations. The authors would also like to thank Andre Tayamen for his assistance 3D printing parts and acting as a beta tester for the instrument.

Funding

This work was funded by a grant from SES AI.

Supplementary materials

Supplementary material associated with this article can be found, in the online version, at doi:10.1016/j.electacta.2025.146012.

Data availability

Code is accessible on the Github page linked in the paper. Data is available upon request.

References

[1] J. Tan, D. Liu, X. Xu, L. Mai, In situ/operando characterization techniques for rechargeable lithium-sulfur batteries: a review, Nanoscale 9 (2017) 19001–19016, https://doi.org/10.1039/c7nr06819k.
[2] M.B. Dixit, J.-S. Park, P. Kenesei, J. Almer, K.B. Hatzell, Status and prospect of in situ and operando characterization of solid-state batteries, Energy Environ. Sci. (2021), https://doi.org/10.1039/d1ee00638j.
[3] C. Gervillié-Mouravieff, W. Bao, D.A. Steingart, Y.S. Meng, Non-destructive characterization techniques for battery performance and life-cycle assessment, Nat. Rev. Electr. Eng. 18 (1) (2024) 547–558, https://doi.org/10.1038/s44287-024-00069-y, 2024.
[4] Z. Deng, X. Lin, Z. Huang, J. Meng, Y. Zhong, G. Ma, Y. Zhou, Y. Shen, H. Ding, Y. Huang, Recent progress on advanced imaging techniques for lithium-ion batteries, Adv. Energy Mater. 11 (2021) 2000806, https://doi.org/10.1002/AENM.202000806.
[5] G. Qian, S. Kuppan, A. Gallo, J. Zhou, Z. Liu, Y. Liu, From in-situ experimentation to in-line metrology: advanced imaging characterization for battery research and manufacturing, Energy Storage Mater. 73 (2024) 103819, https://doi.org/10.1016/J.ENSM.2024.103819.
[6] M.E. McGovern, D.D. Bruder, E.D. Huemiller, T.J. Rinker, J.T. Bracey, R.C. Sekol, J. A. Abell, A review of research needs in nondestructive evaluation for quality verification in electric vehicle lithium-ion battery cell manufacturing, J. Power Sources 561 (2023) 232742, https://doi.org/10.1016/J.JPOWSOUR.2023.232742.
[7] K. Hatzell, W. Chang, W. Bao, M. Cai, T. Glossmann, S. Kalnaus, B. Liaw, Y.S. Meng, R. Mohtadi, Y. Wang, Aligning lithium metal battery research and development across academia and industry, Joule 8 (2024) 1550–1555, https://doi.org/10.1016/j.joule.2024.04.007.
[8] Y. Wang, J. Tian, Z. Sun, L. Wang, R. Xu, M. Li, Z. Chen, A comprehensive review of battery modeling and state estimation approaches for advanced battery management systems, Renew. Sustain. Energy Rev. 131 (2020) 110015, https://doi.org/10.1016/J.RSER.2020.110015.
[9] P.J. Withers, C. Bouman, S. Carmignato, V. Cnudde, D. Grimaldi, C.K. Hagen, E. Maire, M. Manley, A. Du Plessis, S.R. Stock, X-ray computed tomography, Nat. Rev. Methods Prim. 11 (1) (2021) 1–21, https://doi.org/10.1038/s43586-021-00015-4, 2021.
[10] N. Meddings, M. Heinrich, F. Overney, J.S. Lee, V. Ruiz, E. Napolitano, S. Seitz, G. Hinds, R. Raccichini, M. Gaberšček, J. Park, Application of electrochemical impedance spectroscopy to commercial Li-ion cells: a review, J. Power Sources 480 (2020) 228742, https://doi.org/10.1016/J.JPOWSOUR.2020.228742.
[11] J.O. Majasan, J.B. Robinson, R.E. Owen, M. Maier, A.N.P. Radhakrishnan, M. Pham, T.G. Tranter, Y. Zhang, P.R. Shearing, D.J.L. Brett, Recent advances in acoustic diagnostics for electrochemical power systems, J. Phys. Energy 3 (2021) 032011, https://doi.org/10.1088/2515-7655/ABFB4A.
[12] Y. Wang, X. Lai, Q. Chen, X. Han, L. Lu, M. Ouyang, Y. Zheng, Progress and challenges in ultrasonic technology for state estimation and defect detection of lithium-ion batteries, Energy Storage Mater 69 (2024) 103430, https://doi.org/10.1016/J.ENSM.2024.103430.
[13] A.G. Hsieh, S. Bhadra, B.J. Hertzberg, P.J. Gjeltema, A. Goy, J.W. Fleischer, D. A. Steingart, Electrochemical-acoustic time of flight: in operando correlation of physical dynamics with battery charge and health, Energy Environ. Sci. 8 (2015) 1569–1577, https://doi.org/10.1039/C5EE00111K.
[14] G. Davies, K.W. Knehr, B. Van Tassell, T. Hodson, S. Biswas, A.G. Hsieh, D. A. Steingart, State of charge and State of health estimation using electrochemical acoustic time of flight analysis, J. Electrochem. Soc. 164 (2017) A2746–A2755. https://iopscience.iop.org/article/10.1149/2.1411712jes (accessed February 26, 2024).
[15] W. Chang, D. Steingart, Operando 2D acoustic characterization of lithium-ion battery spatial dynamics, ACS Energy Lett 6 (2021) 2960–2968, https://doi.org/10.1021/ACSENERGYLETT.1C01324/SUPPL_FILE/NZ1C01324_SI_009.MP4.
[16] Z. Deng, Z. Huang, Y. Shen, Y. Huang, H. Ding, A. Luscombe, M. Johnson, J. E. Harlow, R. Gauthier, J.R. Dahn, Ultrasonic scanning to observe wetting and "unwetting" in Li-ion pouch cells, Joule 4 (2020) 2017–2029, https://doi.org/10.1016/j.joule.2020.07.014.
[17] D. Wasylowski, H. Ditler, M. Sonnet, T. Falkenstein, L. Leogrande, E. Ronge, A. Blömeke, A. Würsig, F. Ringbeck, D.U. Sauer, Operando visualisation of lithium plating by ultrasound imaging of battery cells, Nat. Commun. 151 (15) (2024) 1–11, https://doi.org/10.1038/s41467-024-54319-6, 2024.
[18] W. Chang, C. Bommier, T. Fair, J. Yeung, S. Patil, D. Steingart, Understanding adverse effects of temperature shifts on Li-ion batteries: an operando acoustic study, J. Electrochem. Soc. 167 (2020) 090503. https://iopscience.iop.org/article/10.1149/1945-7111/ab6c56 (accessed February 26, 2024).

[19] C. Bommier, W. Chang, Y. Lu, J. Yeung, G. Davies, R. Mohr, M. Williams, D. Steingart, In operando acoustic detection of lithium metal plating in commercial LiCoO2/graphite pouch cells, Cell Reports Phys. Sci. 1 (2020). http://www.cell.com/article/S2666386420300254/fulltext (accessed February 26, 2024).
[20] A. Fordham, Z. Milojevic, E. Giles, W. Du, R.E. Owen, S. Michalik, P.A. Chater, P. K. Das, P.S. Attidekou, S.M. Lambert, P.K. Allan, P.R. Slater, P.A. Anderson, R. Jervis, P.R. Shearing, D.J.L. Brett, Correlative non-destructive techniques to investigate aging and orientation effects in automotive Li-ion pouch cells, Joule 7 (2023) 2622–2652. http://www.cell.com/article/S2542435123004403/fulltext (accessed July 23, 2024).
[21] H. Huo, K. Huang, W. Luo, J. Meng, L. Zhou, Z. Deng, J. Wen, Y. Dai, Z. Huang, Y. Shen, X. Guo, X. Ji, Y. Huang, Evaluating interfacial stability in solid-State pouch cells via ultrasonic imaging, ACS Energy Lett. 7 (2022) 650–658, https://doi.org/10.1021/ACSENERGYLETT.1C02363/SUPPL_FILE/NZ1C02363_SI_005.MP4.
[22] L. Yan, X. Zang, Z. Nie, L. Zhong, Z.D. Deng, W. Wang, Online and noninvasive monitoring of battery health at negative-half cell in all-vanadium redox flow batteries using ultrasound, J. Power Sources 580 (2023) 233417, https://doi.org/10.1016/J.JPOWSOUR.2023.233417.
[23] S. Montoya-Bedoya, E. Garcia-Tamayo, D. Rohrbach, J.P. Gaviria-Cardona, H. V. Martinez-Tejada, B. Planden, D.A. Howey, W.F. Florez, R.A. Valencia, M. Bernal, Quantitative ultrasound spectroscopy for screening cylindrical lithium-ion batteries for second-life applications, Batter. Supercaps 7 (2024), https://doi.org/10.1002/batt.202400002.
[24] P.J. Shull, B.R. Tittmann, Ultrasound, in: P.J. Shull (Ed.), Nondestruct. Eval. Theory, Tech. Appl., CRC Press, New York, 2002: pp. 63–192.
[25] L.W. Schmerr, Fundamentals of Ultrasonic Nondestructive Evaluation, Springer US, Boston, MA, 1998. https://doi.org/10.1007/978-1-4899-0142-2.
[26] L. Gold, T. Bach, W. Virsik, A. Schmitt, J. Müller, T.E.M. Staab, G. Sextl, Probing lithium-ion batteries' state-of-charge using ultrasonic transmission – Concept and laboratory testing, J. Power Sources 343 (2017) 536–544, https://doi.org/10.1016/J.JPOWSOUR.2017.01.090.
[27] L.P. Bauermann, L.V. Mesquita, C. Bischoff, M. Drews, O. Fitz, A. Heuer, D. Biro, Scanning acoustic microscopy as a non-destructive imaging tool to localize defects inside battery cells, J. Power Sources Adv. 6 (2020) 100035, https://doi.org/10.1016/J.POWERA.2020.100035.
[28] R.J. Copley, R.S. Dwyer-Joyce, Prediction of the internal structure of a lithium-ion battery using a single ultrasound wave response, J. Energy Storage 72 (2023) 108778, https://doi.org/10.1016/J.EST.2023.108778.
[29] K.L. Williams, An effective density fluid model for acoustic propagation in sediments derived from Biot theory, J. Acoust. Soc. Am. 110 (2001) 2276–2281, https://doi.org/10.1121/1.1412449.
[30] D. Wasylowski, N. Kisseler, H. Ditler, M. Sonnet, G. Fuchs, F. Ringbeck, D.U. Sauer, Spatially resolving lithium-ion battery aging by open-hardware scanning acoustic imaging, J. Power Sources 521 (2022) 230825, https://doi.org/10.1016/J.JPOWSOUR.2021.230825.
[31] GitHub - changbatterygroup/ultrasonicTesting: testing code for running ultrasonic experiments, (n.d.). https://github.com/changbatterygroup/ultrasonicTesting (accessed December 12, 2024).
[32] pickle — Python object serialization — Python 3.13.1 documentation, (n.d.). https://docs.python.org/3/library/pickle.html (accessed December 12, 2024).
[33] R.E. Owen, J.B. Robinson, J.S. Weaving, M.T.M. Pham, T.G. Tranter, T.P. Neville, D. Billson, M. Braglia, R. Stocker, A.A. Tidblad, P.R. Shearing, D.J.L. Brett, Operando Ultrasonic monitoring of lithium-ion battery temperature and behaviour at different cycling rates and under drive cycle conditions, J. Electrochem. Soc. 169 (2022) 040563, https://doi.org/10.1149/1945-7111/AC6833.
[34] N. Kaden, R. Schlimbach, Á.Rohde García, K. Dröder, A systematic literature analysis on electrolyte filling and wetting in lithium-ion battery production, Batteries 9 (2023) 1–22, https://doi.org/10.3390/batteries9030164.
[35] F.J. Günter, J.B. Habedank, D. Schreiner, T. Neuwirth, R. Gilles, G. Reinhart, Introduction to electrochemical impedance spectroscopy as a measurement method for the wetting degree of lithium-ion cells, J. Electrochem. Soc. 165 (2018) A3249–A3256, https://doi.org/10.1149/2.0081814jes.